PNAS

Main Manuscript for

Reconfiguration of brain-wide neural activity after early life adversity.

Taylor W. Uselman[1], Russell E. Jacobs[2,3], Elaine L Bearer[1,3]

[1] University of New Mexico Health Sciences Center, Albuquerque, NM 87131
[2] Zilkha Neurogenetic Institute, Keck School of Medicine of University of Southern California, Los Angeles, CA 90033
[3] California Institute of Technology, Pasadena, CA 91125

Corresponding Author: Elaine L. Bearer
Email: elaine.bearer@gmail.com; ebearer@salud.unm.edu

Author Contributions: T.W.U. performed research, contributed analytical tools, analyzed data and wrote the paper; R.E.J. designed and performed research, developed the imaging protocol, analyzed data and edited the manuscript; E.L.B. designed and performed research, analyzed data, wrote and edited the manuscript.

Competing Interest Statement: The authors declare no competing interests.

Classification: Biological Sciences (Major), Neuroscience (Minor).

Keywords: manganese-enhanced magnetic resonance imaging, brain states, neuroimaging, early life adversity, acute threat

This PDF file includes:

Main Text
Figures 1 to 6
Table 1

Abstract

Early life adversity (ELA) predisposes individuals to both physical and mental disorders lifelong. How ELA affects brain function leading to this vulnerability is under intense investigation. Research has begun to shed light on ELA effects on localized brain regions within defined circuits. However, investigations into brain-wide neural activity that includes multiple localized regions, determines relationships of activity between regions and identifies shifts of activity in response to experiential conditions is necessary. Here, we performed longitudinal manganese-enhanced magnetic resonance imaging (MEMRI) to image the brain in normally reared or ELA-exposed adults. Images were captured in the freely moving home cage condition, and short- and long-term after naturalistic threat. Images were analyzed with new computational methods, including automated segmentation and fractional activation or difference volumes. We found that neural activity was increased after ELA compared to normal rearing in multiple brain regions, some of which are involved in defensive and/or reward circuitry. Widely distributed patterns of neural activity, “brain states”, and their dynamics after threat were altered with ELA. Upon acute threat, ELA-mice retained heightened neural activity within many of these regions, and new hyperactive responses emerged in monoaminergic centers of the mid- and hindbrain. Nine days after acute threat, heightened neural activity remained within locus coeruleus and increased within posterior amygdala, ventral hippocampus, and dorso- and ventromedial hypothalamus, while reduced activity emerged within medial prefrontal cortical regions (prelimbic, infralimbic, anterior cingulate). These results reveal that functional imbalances arise between multiple brain-systems which are dependent upon context and cumulative experiences after ELA.

Significance Statement

Early life adversity (ELA) is a crucial determinant of adult health. Yet, the neurobiological basis for this association remains elusive. Neural activity differs within localized brain regions in rodents who experienced ELA, yet how this localized activity contributes to overall brain states has hitherto been unknown. Here we used longitudinal manganese-enhanced MRI to reveal brain-wide activities altered by ELA compared to normal rearing. Advanced computational analyses unveiled widespread reconfiguration of segment-wise neural activity throughout the brain across a series of conditions: freely moving, experiencing threat or its aftermath. These brain state dynamics were unique to ELA. Reconfiguration of brain states after ELA, shown here for the first time, may underlie predisposition to mental and physical disorders after childhood adversity.

Main Text

Introduction

Early life adversity (ELA) poses risks for neuropsychiatric disorders, especially after a second traumatic event (1-5). Several theories have emerged as to ELA's long-term consequences on global neural activity into adulthood. These changes are likely to contribute to the biological underpinnings for poor mental health outcomes.

Results from studies measuring neural activity in discrete regions within the brain report altered physiology associated with ELA (6-10). These alterations may be found within reward and defensive circuits (11-14). Fragmented maternal care, a paradigm for ELA in rodents (15, 16) which we use here, results in hyperactivity in corticotropin-releasing neurons within the hypothalamus in mice (17, 18). Physiological changes in additional sub-regions have been found in other experiments using various methods to produce ELA and to measure physiology (6-10). These studies point to alterations throughout the brain, including within amygdala (19, 20), medial prefrontal cortex (PFC) (21, 22), and nucleus accumbens (23). Many questions remain. How do these sub-regions relate, what other regions are involved, and how does activity change in response to a secondary traumatic event, such as a threat? A longitudinal brain-wide imaging strategy followed by automated, unbiased, comprehensive, data-driven analyses is needed to address these questions.

Longitudinal manganese-enhanced MRI (MEMRI) together with computational processing fills this need. MEMRI uniquely detects brain-wide neural activity (24-29) or axonal projections (30-37) in freely moving mice and can be repeatedly applied at defined intervals before, during, and after an experience. Mn(II) administered systemically distributes throughout the brain parenchyma (24), enters active neurons through voltage gated calcium channels (38, 39) and accumulates in neurons in an activity-dependent manner (25, 40, 41). Mn(II)'s robust hyperintense signal represents a composite picture of neural activity occurring between systemic delivery and imaging. Unlike other methods, such as electrophysiology, calcium imaging, optogenetics and histology, MEMRI is non-invasive and non-destructive and can be used repeatedly (25, 42). Thus, MEMRI offers a unique option, with all the necessary features, to image enduring consequences of ELA on brain-wide activity in the adult brain and its dynamics in response to threat.

We previously reported applying this imaging strategy to study the impact on brain-wide activity of predator odor (29), a well-established paradigm for naturalistic innate threat responses (43-45). We

found active regions both within and beyond threat and reward circuits after a single acute threat experience at both short and long-term using statistical mapping. In fMRI studies, activation volumes, defined as statistically enhanced voxels, correlate with functionally relevant outcomes (46). We developed an automated volumetric analysis (46-48) based on MEMRI data (29). This analysis identified segment-wise "fractional activation volumes," the fraction of total voxels within each brain segment that were significantly enhanced. Our longitudinal procedure revealed that the relative sizes of the activation volumes between segments shifted with condition. For example, during acute threat, both lateral amygdala (LA) and bed nucleus of the stria terminalis (BST) were 20% active, a fraction (0.2) of total segment volumes, whereas 9 days later LA had zero activity and BST was 40% active (0.4 fractional activation volume). Serotonin transporter gene knockout affected these patterns. Here we define these anatomical distributions of fractional activation volumes as representing "brain states", which are widely distributed patterns of brain activity evoked by specified conditions that affect future physiology and are modified by neuromodulatory tone (49).

Here, we examine consequences of ELA on adult brain-wide activity during normal home cage exploration in the adult and investigate how this activity changes in response to acute threat, short and long term, with data-driven and hypothesis-based analyses of MEMRI images captured longitudinally. We explore the balance of fractional activation volumes between 96 segments under each condition and how this differs with ELA. We deploy our MEMRI-computational analyses to delineate brain states reconfigured by ELA and their relationship to those evoked by threat.

Results

Longitudinal Imaging Strategy. Adult mice, who had been previously reared either with or without ELA, were imaged by MEMRI before, immediately and long-term after a single acute threat (**Fig. 1A**). ELA was produced according to an established fragmented maternal care paradigm, where dams are provided with limited bedding and nesting material from post-natal day P2 to P9 (16). Acute threat was provoked using a naturalistic predator odor paradigm with TMT, a synthetic odor derived from the fox anal gland (43, 45). After reaching adulthood (~3 months) in standard housing, mice were first video recorded as they explored a custom arena. Then a non-enhanced Pre-Mn baseline MR image (BL-PreMn) was collected. After systemic injection of $MnCl_2$, mice were returned to their home cage for 22h, allowing time for Mn(II) to distribute throughout the brain, accumulate in active neurons and be available to label additional activity. After capture of a post-$MnCl_2$ image, representing the home cage condition (HC), mice were again placed in the arena, recorded while exposed to threat (TMT), and then rescanned to detect the immediate effect on

107 localized Mn(II)-uptake. Finally, eight days after the first Mn(II) injection, another session in the
108 arena was recorded and an MR image captured to detect signal from any residual Mn(II) (D9-
109 PreMn). Mice were then injected a second time with $MnCl_2$, returned to the home cage overnight
110 and scanned ~24h later to detect new or sustained neuronal activity (D9), with the same post-$MnCl_2$
111 interval as the previous post-$MnCl_2$ image taken for threat (TMT). This last scan captures brain
112 activity "long-term" after threat (***SI Appendix*** **Table S1**).
113
114 Measurements of exploration show successful re-enactment of the paradigms for ELA and threat
115 (**Fig. 1B**). ELA exposure increases while predator odor decreases exploration of C57BL/6 mice as
116 measured in distance traveled within a lighted arena as previously reported (43, 45, 50, 51).
117 Therefore, to check whether we had faithfully replicated these paradigms, we compared exploration
118 of our mice to these previous reports. We calculated distance traveled per ten-minute interval at
119 baseline prior to the start of experiments (BL-PreMn), during threat exposure (TMT), and at eight
120 days afterward, before the second $MnCl_2$ injection (D9-PreMn). As anticipated, ELA-exposed mice
121 (ELA) traveled significantly greater distances than normally reared mice (Normal) at baseline (BL-
122 PreMn) ($p<0.041$). As expected, a single acute threat exposure (TMT) significantly reduced
123 distance traveled regardless of rearing in both groups ($p<0.0001$). Nine days after threat (D9-
124 PreMn), both groups increased exploration from their lows during threat (Normal, $p<0.0075$; ELA p
125 < 0.007), with Normal returning to their baseline (no significance difference), and ELA not quite
126 reaching their own baseline high (ELA, D9-PreMn vs BL-PreMn: $p = 0.027$). ELA's greater motility
127 compared to Normal at D9-PreMn approached significance ($p<0.185$). Variance within groups was
128 minimal, ranging from 0.12-0.28 depending upon condition, as estimated by coefficient of variation.
129 These data support the contention that our procedures faithfully reproduced ELA and threat
130 paradigms.
131
132 **Precision Image Preprocessing and Quality Control.** Our protocol captured 8 sequential images
133 across 12 individuals in each cohort, yielding a total of 192 raw images at 2 million voxels each
134 (**Fig. 1C**). All images progressed together through our semi-automated processing pipeline (25,
135 29), which yielded a combined dataset of skull-stripped, normalized and spatially aligned images
136 for statistical evaluation and comparable between datasets. We carefully considered caveats that
137 could confound accurate measurements, such as differences in Mn(II) dosing, image acquisition
138 parameters, or processing and none were found (***SI Appendix*** **Fig. S1** and **Table S1**).
139
140 **Three Brain States in Mice Exposed to ELA**. We began with statistical parametric mapping
141 (SPM) of our MEMRI datasets of the ELA cohort (**Fig. 2**) (52, 53), since we had already reported
142 similar maps for normally reared mice (29). We compared ELA images from each condition (HC,

143 TMT and D9) with their BL-PreMn image (**Fig. 2A**) (T=5.45, p< 0.0001 *cluster corr.*), to obtain a
144 picture of statistically significant Mn(II) accumulation at each condition not impacted by changes
145 between conditions. At HC most of OLF, striatum and pallidum, as well as various segments within
146 the hypothalamus (HYP), cerebellum (CB) and subsegments of hippocampus (HIP) and amygdala
147 (AMY) were highlighted. After TMT, much of this activity was maintained, while some regions
148 expanded, and new regions, such as locus coeruleus (LC) and central amygdala (CEA), appeared
149 (**Fig. 2B**). Distributed patterns of activity transitioned again at D9, with noticeable decrease of
150 volumes throughout many areas of the brain that were previously active at HC and at TMT (**Fig.**
151 **2C**). The overall volume of activity shrinks, most obviously within OLF and CB regions, while some
152 activity persisted in BST, HIP, and CEA. Of these regions that persisted, only the CEA had no
153 signal in HC. In HYP, sub-region distribution shifted, with activity in some segments decreased
154 while others increased. In HB, significant voxels almost disappeared at D9 in this comparison.
155 Thus, exposure to ELA renders the brain already highly active in the home cage condition within
156 regions associated with threat and reward. Despite this activity, the ELA brain is still capable of
157 responding to a secondary acute threat with further activity. These post-threat patterns resolve, not
158 to the pre-threat baseline, but to a third activity pattern.
159
160 **Magnitude of Signal Enhancements.** We hypothesized that Mn(II) accumulations would increase
161 in ELA in those regions previously reported to respond to predator odor in normally reared mice
162 (11, 12) (**Fig. 3**). We selected candidate ROIs in the olfactory system: main olfactory bulb (MOB),
163 AON, and PIR (11, 54, 55), and measured Mn(II) intensity values before and after threat in our ELA
164 datasets (**Fig. 3A**, and ***SI Appendix*** **Tables S2** and **S3**). Although intensity was already 5.6-8.1%
165 above pre-Mn(II) levels in ELA mice at home cage (HC), it significantly increased after predator
166 odor (TMT) (1.2-1.7%, $p < 0.05$ for each ROI). In three other subdomains (AMY: MEA, CEA, BLA),
167 intensity in ELA increased with TMT (1.8-5.8%, $p<0.05$ for each ROI) as reported in normal (11,
168 12) (**Fig. 3B**).
169
170 Second, we tested the hypothesis that the magnitude of responses differed in ELA from Normal in
171 specific candidate regions implicated in brain-wide threat responses (29). We measured intensity
172 between Normal and ELA groups in six limbic system regions (MOB, NDB, LSr, ACB, BLA, SPA)
173 and performed a 2-way comparison at HC and TMT (**Fig. 3C**, ***SI Appendix*** **Tables S2** and **S4**, and
174 **Fig. S2**). In Normal, TMT exposure increased signal intensity in all six regions, as reported (29). In
175 two regions (LSr and SPA), the levels and dynamics of intensities in ELA differed significantly from
176 Normal, while in another region, only the levels and not the dynamics differed (ACB). In the
177 remaining three regions (MOB, NDB, BLA), intensity increased after TMT in both groups, without
178 significant differences between groups (***SI Appendix*** **Fig. S2**). Thus, responses to threat after ELA,

179 as measured with MEMRI, differ from Normal only in some regions of the brain, emphasizing the
180 need for whole brain analyses.
181
182 **Expression of c-fos Corresponds to Statistically Significant Mn(II)-Enhanced Signal.** At the
183 conclusion of imaging mice were returned to the home cage for several days and then sacrificed,
184 fixed and the brain embedded, sectioned and stained by immunohistochemistry for c-fos, a well-
185 known marker for neural excitation (25, 28, 47, 56) (**Fig. 4**). Thus, we considered c-fos expression
186 to be at basal levels, a close approximation to MEMRI at HC condition. Due to constraints of
187 experimental procedures, it was not possible to perform these two tests precisely parallel, but the
188 same individuals were imaged with both modalities. Anatomical landmarks were visualized in our
189 *InVivo* Atlas (***SI Appendix* Fig. S3**) and matched to those in histologic sections. HYP displayed
190 numerous c-fos positive nuclei in the same regions that had significantly enhanced voxels at HC,
191 including PH, LHA, and STN (**Fig. 4A-D,** SPM set at $p < 0.0001$, $T = 5.45$). In contrast, little to no
192 signal in either SPM or histological images appeared in adjacent segments, such as ZI, MBO, or
193 THA. In those areas where c-fos staining was sparse, significant voxels were also not found by
194 SPM of MEMRI, at this threshold of $p < 0.0001$. In the midbrain, SPM and c-fos staining also
195 correlated. Like HYP, IPN was another region highly active by SPM of MEMRI. As in HYP, IPN
196 displayed a high density of c-fos positive nuclei while most of the midbrain not highlighted by SPM
197 was also c-fos negative (**Fig. 4E**). Hence, detection of statistically enhanced voxels by SPM may
198 depend both on degree of activity and density of active cells. C-fos staining at cellular resolution is
199 more sensitive than SPM of MEMRI, as microscopy detecting individual neuronal nuclei is beneath
200 the spatial resolution of MR imaging. On the other hand, SPM did not find signal in regions that
201 lacked c-fos staining, *i.e.,* MEMRI does not produce false positive signals by these criteria. All
202 regions with statistically significant enhancement that we examined also displayed a high density
203 of c-fos positivity.
204
205 **Deeper Dives into Brain States of Adult Mice Exposed to ELA.** We overlaid statistical maps
206 from two different comparisons onto the same grayscale template to visualize anatomical
207 differences in global distributions of statistically significant voxels (**Fig. 5, top panels**). Fractional
208 activation volumes per segment are displayed as column graphs (**Fig. 5, lower panels,** also *see*
209 ***SI Appendix* Table S6**). Overlays of statistical maps of HC with TMT of ELA mice showed
210 considerable anatomical overlap as well as both expanding and contracting fractional activation
211 volumes ($p < 0.0001$, $T = 5.45$) (**Fig. 5A).** During normal exploration (HC), many segments had
212 dramatic activity, prominent within four of the ten anatomical domains (OLF, STR/PAL, HYP, and
213 CB). In some of these segments nearly all voxels were active, *e.g.*, MOB, BST, MS, AHN. After
214 acute threat (TMT), large activation volumes at HC were mostly retained or further increased. In a

few segments, fractional activation volumes increased appreciably, *e.g.*, CEA (from 211 voxels at HC to 766 voxels at TMT, 0.14 to 0.51 of total volume) and locus coeruleus LC (from 1 voxel at HC to 29 voxels at TMT, 0.01 to 0.35 of total volume). Activation volumes decreased slightly with TMT in only a small number of segments, *e.g.*, MH and STN. In a select few that had small numbers of total voxels, little activity was found in one of the two conditions, and a reasonably large fraction of activity in the other, *e.g.*, LGd in THA (from 15 voxels at HC to 0 voxels at TMT, 0.25 to 0.0 of total volume) and LC in HB (from 1 voxel at HC to 29 voxels at TMT, 0.01 to 0.35 of total volume). Although SPM detected little activity in either condition in cortex or thalamus at this statistical stringency, some was appreciable at lower T-values (***SI Appendix* Fig. S4**). Comparison between sexes, where ELA is reported to have greater impact in females (57), did not detect major differences from those reported here based on a mixed sex cohort. (***SI Appendix* Fig. S5).**

We then compared segmental activities between acute threat (TMT) and nine days later (D9) in ELA mice (**Fig. 5B**, top panel). Segmentation analysis revealed that activity virtually disappeared in HB and CB and substantially decreased in OLF overall. Conversely, in a subset of segments where activity had been stimulated by acute TMT, activity at D9 either persisted, *e.g.*, CEA (from 766 at TMT to 711 voxels at D9, 0.51 to 0.48), or increased, such as in ZI (from 485 at TMT to 706 voxels at D9, 0.33 to 0.47). A subset of other segments where there was minimal activity after TMT, *e.g.*, MH, STN, VTA, SNc, became highly active at D9. This comparison with HC shows that global activity at D9 in ELA mice was not at pre-threat levels.

To pinpoint which regions differed at the D9 compared to the pre-threat (HC) condition in ELA- and in normally reared mice, we used the same map overlay and segmentation strategy described above (**Fig. 5C and 5D,** also see ***SI Appendix* Table S6**). Qualitative comparison of both maps and column graphs between these two within-group analyses revealed obvious between-group differences. First, prior to threat fractional activation volumes in Normal mice were substantially lower than ELA mice across most of the brain. The increased signal in ELA data could not be explained by any differences in our experimental procedures: amounts of $MnCl_2$ injected, MR scanning parameters, relative timing of imaging, processing pipelines or segmentation analyses (see ***SI Appendix* Fig. S1C and Table S1**). At nine days after threat, normally reared mice had heightened activity relative to HC in multiple segments, *e.g.,* CEA, BST, MPO, STN, VTA, SNc, and IPN (**Fig. 5C**). In contrast, in ELA mice most of the heightened activity at HC prior to threat decreased at D9 (**Fig. 5D**). Some of those segments that increased in Normal mice at D9 decreased in ELA mice, *e.g.*, LSc/r, MPO, and IPN. Thus, in many cases the differences between HC and post-threat were opposite between groups, with Normal being heightened and ELA being diminished after threat, as if threat had dispelled some baseline activity in ELA and brought those

segments closer to the activity of normally reared mice. In other segments, where the volume of activity between pre- and post-threat increased in both groups, the amount of change was substantially greater in ELA, *e.g.,* CEA, SNc, producing an altered brain state between the two groups despite some convergence after a threat experience. These qualitative differences identified by visual comparisons led us to pursue a more direct and quantitative, between-group statistical analysis, despite potentially lower power.

ELA Affects Many Segments Within Each Anatomical Domain. For a direct statistical comparison between ELA and Normal mice at each condition, we used a two-tailed, unpaired SPM design (**Fig. 6**). This analysis produced two voxel-wise maps of significant intensity differences, one with ELA greater than Normal and the other vice-versa ($p < 0.01$, $T = 2.51$, *cluster corr.*) (**Fig. 6, rows A-C, left panels**). These unpaired t-maps only indicate significant differences of voxel-wise intensities between groups and not overall Mn(II) accumulations. This analysis affirmed our impression of heightened activity in the ELA group compared to Normal (**Fig. 5**) and that this difference was significant.

We segmented these unpaired, between-group t-maps to calculate segment-wise "fractional difference volumes," *i.e.*, the fraction of voxels significantly greater in intensity in one group versus the other within a particular segment (**Fig. 6, rows A-C, middle panels**). At all three conditions, many segments in multiple domains of ELA mice had large volumes with intensities significantly greater than Normal: at HC: OLF, STR/PAL, and HYP; at TMT: MB, HB and CB; and at D9: HIP, AMY, HYP, and HB. In contrast, at only one condition, D9, were intensities greater in any domain in Normal than in ELA: CTX (ACA, SS, ORB, MO, and PL, 0.04 - 0.18 of total volumes). Fractional difference volumes within segments were dynamic, increasing or decreasing across conditions seemingly unpredictably (see ***SI Appendix*** **Table S7**). At D9 in ELA, intensity was less than Normal in prefrontal CTX, while greater than Normal in deeper segments: CA1-CA3, PA, DMH and VMH, PCG and LC. Many of these deeper hyperactive segments occupied regions considered to be part of the limbic system (ventral hippocampus, amygdala, hypothalamus) as well as neuromodulatory systems (VTA, DR and LC). Taken together, this data and analysis pinpoint segments within domains with the greatest degree of abnormal activity, both elevated and depressed after ELA (**Table 1**). Widely distributed statistically significant abnormalities in neural activity throughout the brain are the legacy of ELA, as seen in diagrams placing this information in the context of the whole brain (**Fig. 6, rows A-C, right panels**). Each condition has its own balance of activity between domains depending upon rearing (also see ***SI Appendix*** **Fig. S6**). Thus, ELA profoundly alters the unprovoked (resting) brain state in freely moving adult mice and further impacts the trajectory of brain state dynamics associated with threat.

287

288 **Discussion**

289

290 In this study we mapped the spatial-temporal transformations that ELA imposes on brain-wide
291 activity, as detected initially when in a home cage environment and then short and long-term after
292 challenge by an acute threat. Six different brain states (49), as defined here by widely distributed
293 patterns of fractional activation volumes among segments, emerged. In all three conditions, brain
294 states of adult mice reared in the fragmented maternal care model for ELA differed from those with
295 normal rearing, with greater overall neural activity after ELA. Even without any other provocation,
296 adult ELA mice in the home cage had heightened fractional activation volumes in regions known to
297 be activated by predator odor or altered in reward processing: olfactory and hypothalamic segments
298 (56, 58-63), as well as striatum-pallidum (14, 29, 64). In both cohorts, distribution of heightened
299 activity expanded immediately after threat to engage subcortical structures as well as
300 monoaminergic nuclei and deeper brainstem segments. The brain state of ELA mice in home cage
301 condition resembled that of normally reared mice nine days after threat. Although there were many
302 changes from threat to nine days later, neither group regained home cage activity patterns. In many
303 instances, changes at nine days after threat were in opposite directions between groups. While
304 these changes brought the two rearing groups into a more similar brain state, critical differences
305 were notable. Across all conditions, activity in hypothalamus remained higher than normal in ELA
306 reared mice. In contrast, only nine days after threat was ELA significantly different from normal.
307 This difference occurred in segments within prefrontal cortex, where activity was lower than normal,
308 and in ventral hippocampus and posterior amygdala, where activity was greater. Our longitudinal
309 brain-wide imaging strategy coupled with our MEMRI-specific mouse brain atlas (*InVivo* Atlas) and
310 our computational processing and analytics empowered us to follow these anatomically delineated
311 brain states in the same individuals as they transitioned through this series of experiences.

312

313 We found dynamic changes in segment-wise fractional activation volumes throughout the brain in
314 both cohorts, whether they experienced ELA or not. We interpret these dynamics as representing
315 functional changes. We predict that when a segment transitions from lower to higher fractional
316 activation volumes, *e.g.*, as in CEA increasing from 0.14 to 0.51 fraction of total volume from home
317 cage to immediately after threat, we expect that particular segment to have a more dominant role
318 within its connectome, the possible set of functional interactions, one of which for CEA would be
319 within the neural circuit of innate fear (11). Conversely, when fractional activation volumes decrease
320 between conditions, *e.g.,* as in LSr decreasing from 0.64 to 0.17 of total volume from acute threat
321 to D9, that may indicate a decline at D9 of that segment's contribution to the global brain network
322 (65, 66). Differing magnitudes of fractional activation volumes between segments within a single

network, *i.e.*, the relative balance of activities among network components, under different conditions could lead to alternate outcomes from that same network, be they actions, decisions, emotions, thoughts, memories, or creative works, such as music, poetry, or art.

Neuromodulatory systems may manage these disparate activity patterns, by dampening down some segments and stimulating others under different conditions (67-74). ELA is frequently hypothesized to disrupt monoaminergic modulation of brain-states (6-8, 75, 76). Here, we found that ELA predisposed all three monoaminergic systems to respond more robustly to acute threat than in Normal mice, where heightened fractional activation volumes and fractional difference volumes in serotonergic and noradrenergic centers of ELA mice were most prominent. Such modulatory brain centers were identified as both structural and functional network hubs that may enable communication between sub-networks and transitions between brain states (67, 71, 77). We observed threat-induced monoaminergic activations in all three monoaminergic segments (VTA, CS, and LC) which may indicate involvement in the shift in brain states from the home cage condition prior to threat to the same home cage condition nine days after threat.

The results imply that activity might be highly regulated for responses to be appropriate to the situation. Unbalanced activity could result in cognitive impairment, poor decision-making or uncontrollable emotional upsets. Existing treatments for a range of mental illnesses typically target the neuromodulatory systems (78-80), supporting this idea. We show here that a threat experience destabilizes the balance of activity between brain segments of normally reared mice, *i.e.*, the normal brain state, and this may be in part an underlying biology leading to stress-disorders and vulnerability to drug use after threat. That this brain wide destabilization is greater in adult mice with adverse early life experience seems to coincide with observations of similar effects of adverse childhood experiences (ACEs) in humans (10, 81). Longitudinal and retrospective studies in human (82, 83) may help to further attribute these effects across species (84).

Results presented here should be considered in the light of several limitations. These include whether Mn(II) signal faithfully represents neural activity and whether fractional activation leads to physiological outcomes. Staining by c-fos (28, 29) and work by others (28, 38-41, 85, 86) contend that Mn(II) tags active neurons, while electrophysiology will likely be necessary to confirm functional relevance of fractional activities. While sex differences have been described after ELA (57, 87), MEMRI may not be sensitive enough to detect them. Anatomical variations could influence our results (88-91), but by preserving intensity concentrations within brain volumes in our alignments, *i.e.*, no intensity modulation by changes in brain shape, this possibility is minimized (52, 53). Finally,

358 alternative behavioral paradigms for inducing ELA and stress exist (92-97). We chose limited
359 bedding and nesting, and predator odor. Our data may only pertain to those specific paradigms.
360
361 In conclusion, ELA has a global impact on the balance of fractional neural activity among widely
362 distributed sub-regions under all conditions, from normal exploration in the home cage to immediate
363 and post-threat states. We identify specific subcomponents of this global brain network that are
364 differentially activated depending upon condition in adult mice after ELA. Future studies will be
365 useful to dissect functional connections suggested by these MEMRI results. A next step will be to
366 determine the functional significance of these segmental activities, how they interact to reconfigure
367 future brain state topology in response to experience, and whether these interactions underlie
368 vulnerabilities to mental health disorders and/or drug use. Ultimately these studies will lead to an
369 understanding of neurophysiological/biochemical mechanisms contributing to the reconfiguration
370 of brain states by ELA and inspire reparative/restorative interventions to protect from the harm of
371 traumatic events in adulthood.
372
373 **Materials and Methods**
374
375 **Animals and ELA.** All animal protocols were approved by Institutional Animal Care and Use
376 Committees (IACUCs) at both California Institute of Technology and University of New Mexico.
377 Animal numbers were determined by a statistical power analysis. For ELA, pregnant C57BL/6J
378 mouse dams were ordered from Jackson Labs (Stock No: 000664), pregnancy confirmed, and then
379 shipped during gestational days 11-15 and acclimated for at least 1 week in Caltech's animal care
380 facility. Pregnant dams were monitored daily. Upon birth, the number of pups were limited to five
381 per dam. On post-natal day P2, dams and pups were placed in a cage with mesh flooring and
382 provided with 1/3rd of the standard amount bedding and nesting material (15, 16). Mice remained
383 undisturbed from P2 through P9. On P10, dams and pups were returned to standard rearing
384 conditions. Pups were then aged under normal 12h-light-dark cycles within animal care facility until
385 11-13 weeks of age. Equal numbers of male (n = 6) and female (n=6) ELA pups were used. For
386 comparisons to normal rearing, we mined data from 12 male C57BL/6J mice from Uselman, Barto,
387 et al., 2020 (29).
388
389 **Video Recordings and Acute Threat Paradigm**. Mice were placed in a custom arena containing
390 a gauze pad with either saline or TMT (2,3,5-Trimethyl-3-thiazoline), a synthetic odor derived from
391 the fox anal gland that is a naturalistic innate threat for rodents (43, 45). The arena was placed
392 within a chemical fume hood and was wiped down with 70% ethanol before and after every
393 recording to prevent TMT fume contamination between sessions. Mice were video recorded, and

394 movements tracked with Noldus Ethovision (XT15) during the last 10 min of 30 min recordings, as
395 described (29, 98, 99). Distance traveled was analyzed using Ethovision and statistically evaluated
396 in R 4.2.1 using linear mixed models (*nlme*) with Tukey adjusted post-hoc comparisons (*emmeans*)
397 (100-105). Graphs were generated in R (*ggplot2*) (106).
398
399 **Longitudinal MEMRI.** We designed the longitudinal MEMRI procedure to be near identical to our
400 previous report on normally reared mice (29) to enable cross-sectional statistical comparison. We
401 imaged adult ELA mice (10-13 weeks) first without contrast, and then injected them intraperitoneal
402 (i.p.) with 0.3 mmol/kg of $MnCl_2$-$4H_20$ in buffered saline. Imaging was performed in an 11.7 T 89
403 mm vertical bore Bruker BioSpin Avance DRX500 scanner (Bruker BioSpin Inc, Billerica, MA) with
404 a Micro2.5 gradient system, and custom 35 mm linear birdcage radio frequency (RF) coil. Each
405 animal was anesthetized with low levels of isoflurane (1-2% vol/vol in room air) for live imaging.
406 Respiration and temperature were monitored for normal ranges of 100-120 breaths/min and 37° C.
407 Movement within the scanner was minimized by securing the animal's head to a Teflon®
408 stereotaxic unit within the RF coil (29, 32, 107, 108). We employed a T_1-weighted Fast Low Angle
409 Shot (FLASH) imaging sequence (109, 110) with 8 averages, a TR/TE_{eff} = 25 ms/5 ms, and 20°
410 flip-angle. We acquired 100 µm isotropic voxel resolution with a matrix size of 200 x 124 x 82, FOV
411 of 20.0 mm x 12.4 mm x 8.2 mm and a scan time of 34 min. For post-TMT, four consecutive 34 min
412 scans were obtained and averaged (111). Between scanning sessions, video recordings, or $MnCl_2$
413 injections mice were returned to their home cage under standard housing conditions. Thus, 5 MRI
414 sessions were performed, and 8 total images collected for each animal, yielding datasets of 96 total
415 images for each group (ELA and Normals).
416
417 **MR Image Processing and SPM Analysis.** MR images from both groups processed together
418 beginning with N3-correction and skull-stripping (25, 111-113). A linear affine alignment to the
419 dataset average was performed using SPM *Realign* function (52). After modal scaling of intensity
420 values with one of the pre-injection images as template (111), non-linear warping was applied (52).
421 Modal scaling assumes that the majority of voxels within an image are minimally enhanced by
422 Mn(II), thereby enabling detection of voxels with greater degrees of Mn(II)-enhancement. After
423 warping all images were averaged to produce the minimal deformation template for atlas alignment.
424 All images were then smoothed with a 0.3 mm Gaussian kernel. Voxel-wise T maps of statistically
425 significant differences between conditions (paired t-test) or between groups (unpaired t-test) were
426 calculated using SPM12 (53). Statistical maps were cluster corrected (*cluster corr.*) in FSL with a
427 minimum cluster size of 50 voxels and $p < 0.001$ (114).
428

429 **Calculation of the Fraction of Active to Total Voxels per Segmented Brain Region.** Brain
430 images were segmented into 117 regions based on our updated *InVivo* Atlas (29) (See ***SI***
431 ***Appendix*** **Fig. S3** and **Table S3**). The labeled atlas was aligned to the template using a 12
432 parameter inverse affine transformation, mutual information cost function, and nearest neighbor
433 interpolation in FSL (114-116). The greyscale atlas was then non-linearly aligned to the template
434 and the warp-field applied to the labels in SPM (52). We used *fslmaths* to create masks for each
435 segment based on atlas labels and applied the masks to the statistical maps. We omitted atlas-
436 based white matter tracts from segmental analyses. The number of significantly enhanced voxels
437 (as identified by SPM paired or unpaired t-tests) and the number of total voxels within each segment
438 were counted using *fslstats* (24). The fractions of enhanced to total voxels within each segment
439 was calculated from paired t-tests maps (fractional activation volumes, ***SI Appendix*** **Table S6**) and
440 unpaired t-test maps (fractional difference volumes, ***SI Appendix*** **Table S7**) in R and visualized in
441 column graphs represented as fractions using *ggplot* (105, 106, 117). See ***SI Appendix*** **Extended**
442 **Methods** for formulation of fractional volumes.
443
444 **Measurement and Analysis of MR Intensities.** Measurements were made from pre- and post-
445 Mn(II)-enhanced MR images that had been processed for SPM as above. Coordinates (x/y/z) for
446 regions of interest (3x3x3 voxels) were selected by projecting the annotated atlas labels onto the
447 aligned greyscale template in FSLeyes and placing the crosshairs within segments that
448 corresponded to previously reported regions (11, 29). Coordinates were listed in a feeder script
449 that directed other custom scripts to extract mean intensities for multiple ROIs in image stacks
450 using *fslroi*, *fslmaths*, and *fslstats* functions (114). Output was compiled into a csv file using Python
451 for loading into R, where intensity values were converted to percent of signal intensity over pre-
452 Mn(II) baseline. Linear mixed models (*nlme*) compared intensities between conditions or rearing
453 groups (fixed effects), accounting for random effects of individual mice (100-105). See ***SI Appendix***
454 **Table S2** for a list of regions and voxel locations.
455
456 **Immunohistochemistry.** After completion of imaging at D9, mice were housed under standard
457 conditions for 3-4 weeks, underwent an additional imaging series, were returned to standard
458 housing for 3-10 days, and then were deeply anesthetized with avertin (250-500 mg/kg i.p.) (Sigma
459 Aldrich) and subjected to cardiac perfusion using warmed heparinized saline followed by 4%
460 buffered paraformaldehyde. After perfusion, hair and skin were removed and the brain in the skull
461 incubated in fixative overnight. After extraction from the skull the brain was fixed for 1-2 days at 4°
462 C, and then fixative replaced with calcium-magnesium free phosphate buffered saline in 0.01%
463 sodium azide (118). Brains were sent to Neuroscience Associates (NSA)
464 (https://www.neuroscienceassociates.com), embedded in a single block and serially sectioned in

465 register at 35 μm intervals. Sections were collected serially in cups and stained by anti-c-fos
466 immunohistochemistry. Microscopy of sections was performed on an Olympus microscope using
467 CellSens software. Because c-fos expression only lasts about two hours, we assumed that at this
468 timepoint c-fos activity would be at baseline home cage levels.
469
470 **Acknowledgments**
471 We appreciate Christopher S. Medina and Daniel R. Barto for their guidance on image processing
472 protocols; Kathleen Kilpatrick for technical support and histology; Xiaowei Zhang and Sharon Wu
473 Lin for MRI session recordings and animal staff support at Caltech; Kevin P. Reagan and Daniel
474 Perez-Rodriguez for laboratory support, and James Chavez for IT services. We thank Jonathan
475 Brigman, Erik B. Erhard, Natalie Adolphi and Kiran Bhaskar for helpful discussions of procedures,
476 data analysis, and interpretations. We are grateful to Harry B. Gray of the Beckman Institute at
477 Caltech for insights on Mn(II) metallobiology and advice on the manuscript, and to the Beckman
478 Institute at Caltech where MR imaging was performed. Supported by NIH R01MH096093 (ELB),
479 NIH NIA P20AG068077 (ELB), Zilkha Neurogenetic Institute (REJ) and Harvey Family Endowment
480 (ELB).

481 **Figures and Tables**

482 **Figure 1.**

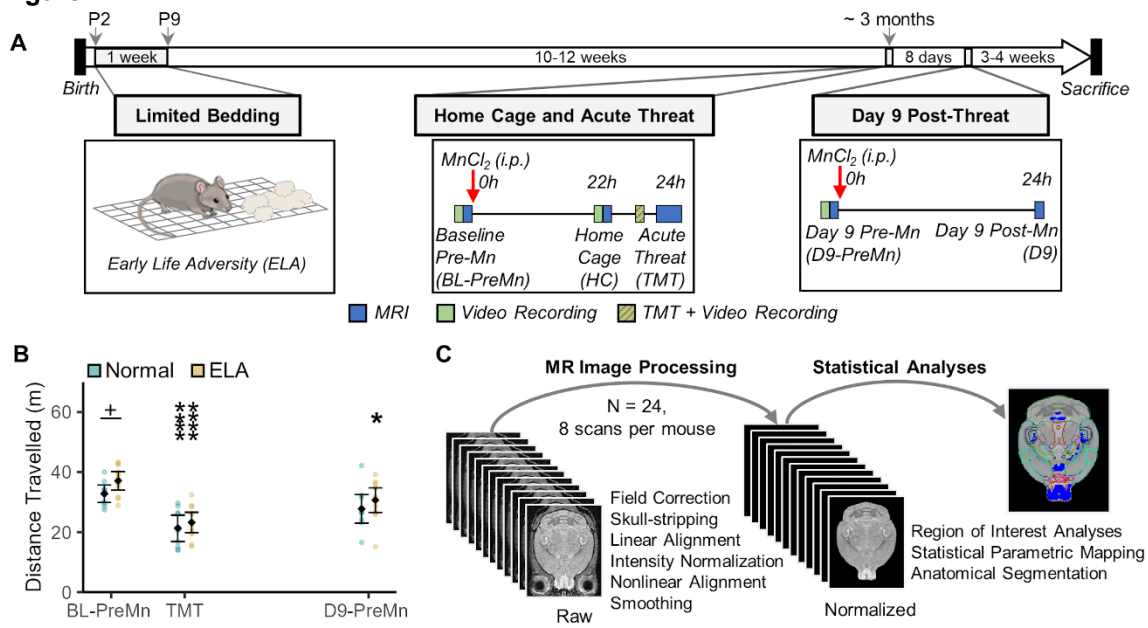

483 **Fig. 1.** Longitudinal MEMRI of adult mice after ELA. (*A*) Schematic of experimental procedures.
484 Timeline shows: post-natal (P) mice and their dams were subjected to limited bedding from P2-P9;
485 Longitudinal MEMRI began in adulthood. In all circumstances outside of ELA, MRI, video
486 recordings, and $MnCl_2$ injections mice were placed under standard housing conditions in their home
487 cage. (*B*) Distance travelled (m) at three timepoints (BL-PreMn, baseline; TMT; and D9-PreMn) in
488 both Normal (cyan) and ELA (yellow) groups (mean ± 95% CI). Fixed effects included condition
489 ($F_{(2,49)} = 24.66$, $p < 0.0001$) and ELA ($F_{(1,49)} = 4.39$, $p < 0.04$). + $p < 0.041$ (post-hoc between group
490 t-test at BL-PreMn, $T_{(49)} = 2.096$). * $p < 0.027$ (pairwise Tukey-adjusted t-test, $T_{(49)} = 9.305$). **** p
491 < 0.0001 (pairwise Tukey-adjusted t-test; Normal, $T_{(49)} = 9.305$; ELA, $T_{(49)} = 9.305$). Pairwise t-tests
492 relative to BL-PreMn. (*C*) Diagram of MR data processing and analysis steps that we deployed in
493 this study (25, 111, 112).

494

495

496 **Figure 2.**

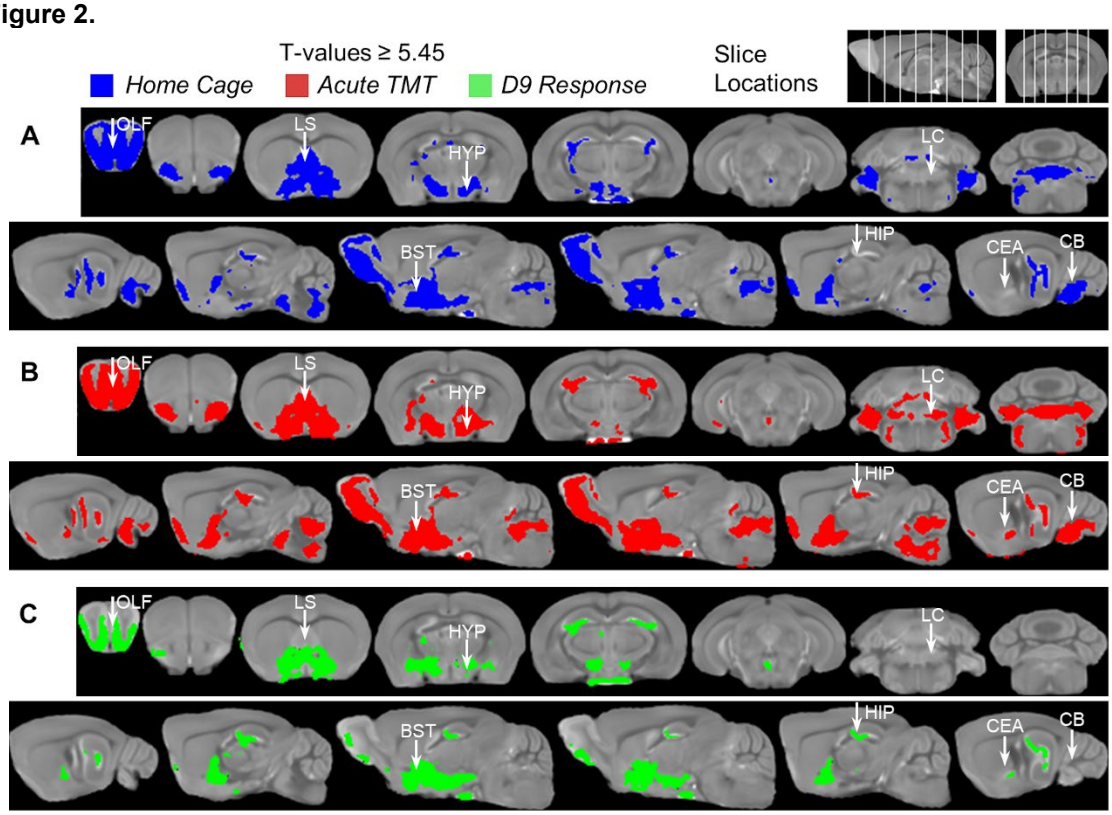

497 **Fig. 2.** Brain-wide voxel-wise statistical parametric maps of Mn(II)-induced signal enhancement.
498 (*A*-*C*) Statistical maps overlaid on the dataset average in both coronal (top rows) and sagittal
499 (bottom rows) orientation (n = 12, $p < 0.0001$, $T > 5.45$, *cluster corr.*). Greyscale orthogonal view
500 with positions of slices (top right) indicated by white lines. White arrows indicate regions with
501 notable enhancement across conditions. OLF, olfactory bulb; LS, lateral septum; BST, bed nuclei;
502 HYP, hypothalamus; HIP, hippocampus; LC, locus coeruleus; CEA, central amygdala; and CB,
503 cerebellum. (*A*) HC (blue), (*B*) TMT (red), (*C*) D9 (green).
504

Figure 3.

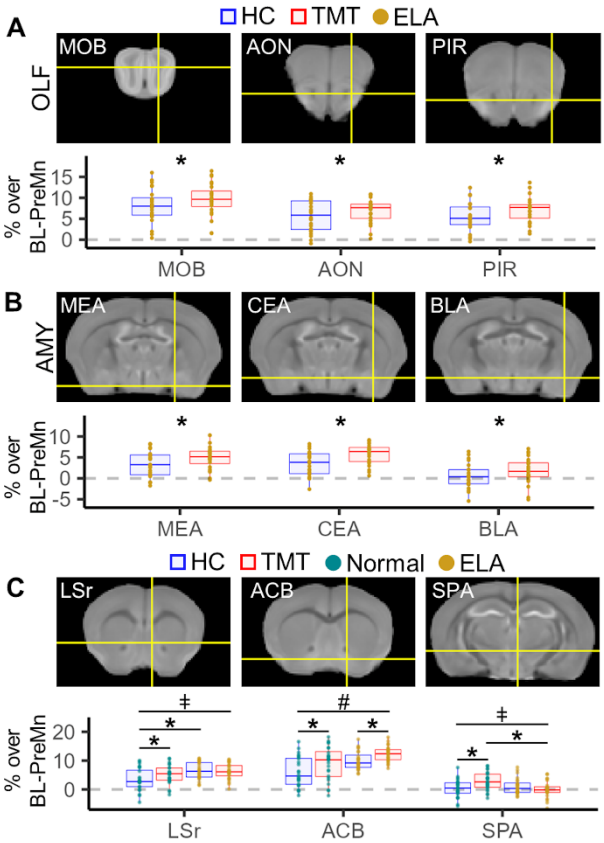

Fig. 3. Magnitude of signal intensity in candidate regions of interest (ROI) that respond to threat. (*A*-*C*) Top panels, MR images with the center of 3x3x3 voxel ROIs indicated by yellow crosshairs from one hemisphere (coordinates listed in ***SI Appendix*** **Table S2**). Lower panels, quartile boxplots of percent signal intensity over BL-PreMn. Individual values from bilateral ROIs as dot plot overlays (summary statistics listed in *SI* ***Appendix*** **Tables S3** and **S4**)

(*A*-*B*) Fixed effect of condition and random effects of individual and hemisphere; * $p < 0.05$, post-hoc paired t-tests. (*A*) Olfactory system comparing HC (blue) to TMT (red). MOB, main olfactory bulb; AON, anterior olfactory nucleus; and PIR, piriform cortex. (*B*) AMY regions comparing HC to TMT. MEA, medial amygdala; CEA, central amygdala; and BLA, basolateral amygdala.

(*C*) Fixed effects of condition and group, comparing three of six regions. HC (blue boxes), TMT (red boxes); Normal (cyan dots), ELA (yellow dots). * post-hoc T-test, $p < 0.05$; # main effect of ELA, $p < 0.05$; ‡ interaction between ELA and condition, $p < 0.05$. For boxplots of other three regions, ***SI Appendix*** **Fig. S2**.

523 **Figure 4.**

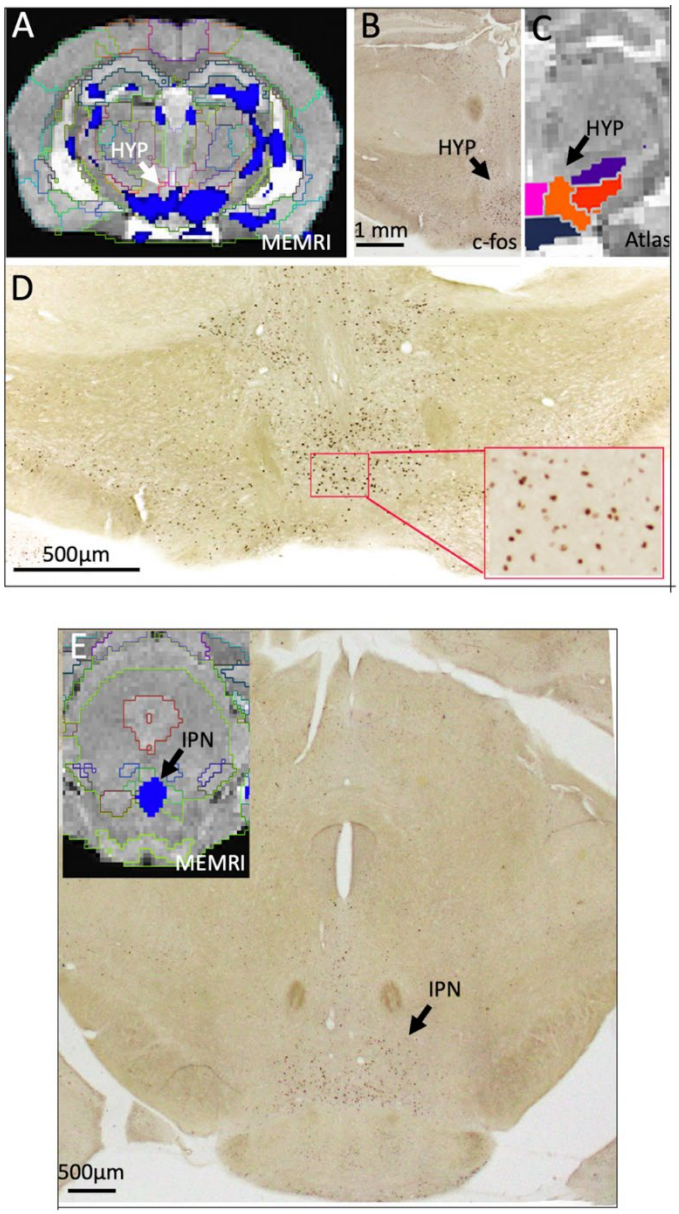

524 **Fig. 4.** Correlations between immunohistochemistry for c-fos and MEMRI. (*A*) Coronal slice of the
525 MR template image overlaid with statistical map of ELA mice at HC ($p < 0.0001$, $T = 5.45$). Note
526 strong signal in the HYP. (*B*) Microscopy at low magnification shows numerous nuclei stained in
527 HYP (mag bar = 1mm). (*C*) Segmented hypothalamic nuclei from our *InVivo* Atlas (pink, PH; orange
528 LHA; red, STN; purple, ZI; black, MBO). For abbreviations see ***SI Appendix*** **Table S5**. (*D*) Higher
529 magnification of image shown in (*B*) (mag bar = 0.5 mm). (*E*) Coronal slice of our grayscale template
530 with statistical overlay from ELA mice at HC condition (blue, statistics as in A) with corresponding
531 histological section through the midbrain. Note activity in IPN in both modalities, while surrounding
532 brain has no significant enhancement in the statistical map. Fewer positive cells appear in

533 segments not highlighted by Mn(II). In (*A)* & (*E)* template images segments are outlined according
534 to our *InVivo* Atlas for anatomical orientation.
535

536 **Figure 5.**

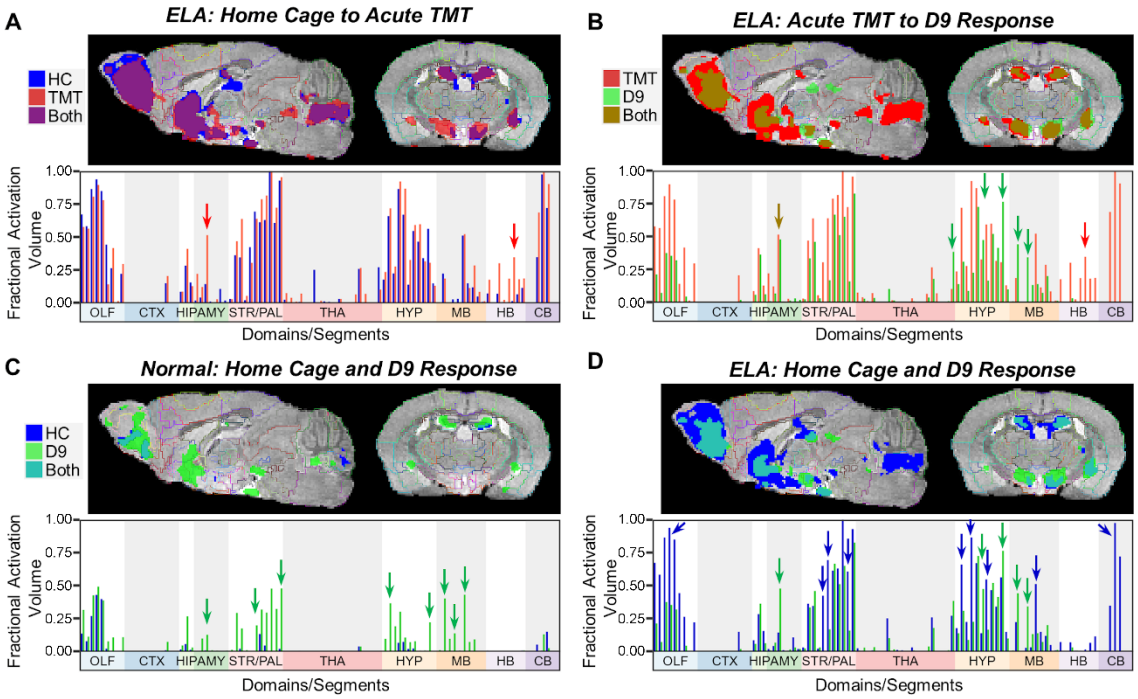

537 **Fig. 5.** Shifts in brain states between conditions. (*A-D*) Statistical maps of paired t-tests projected
538 onto grayscale template with segments outlined for visual comparison of anatomy ($T_{(11)} = 5.45$, $p <$
539 0.0001, *cluster corr.*), corresponding segment-wise column graphs of fractional activation volumes.
540 Horizontal axes represent domains subdivided into 96 segments. See ***SI Appendix*** **Table S5** for
541 domain names and list of segments with abbreviations in order as they appear in the column
542 graphs. Color coding for domains used throughout this paper. See ***SI Appendix*** **Table S6** for
543 fractional activation volume values. (*A-B*) ELA brain states under three conditions. (*C-D*) How brain
544 states at D9 post-threat compare in each group to their HC state.
545
546 (*A*) ELA at HC (blue), and at acute TMT (red), overlap (purple) with corresponding column graph.
547 Red arrows indicate increases in CEA and LC.
548
549 (*B*) ELA at acute TMT (red), and at D9 (green), overlap (brown) with corresponding column graph.
550 Green arrows indicate where fractional activation volumes increase at D9 from TMT: MH, ZI, STN,
551 VTA, and SNc. Note overall decreases in several anatomical domains: OLF, STR/PAL, HB, and

552 CB. Brown arrow indicates CEA where no change from TMT to D9 is detected. Red arrow indicates
553 decrease in LC from TMT to D9.
554
555 (*C*) Normal at HC (blue), and at D9 (green), overlap (cyan) with corresponding column graph. Green
556 arrows indicate segments with minimal activity at HC that increased at D9: CEA, BST, MPO, STN,
557 VTA, SNc, and IPN.
558
559 (*D*) ELA at HC (blue), and at D9 (green), overlap (cyan). Green arrows indicate segments where
560 activity increased over HC to D9: CEA, MH, ZI, STN, VTA, SNc. Blue arrows indicate segments
561 where activity decreased substantially from HC at D9: MOB, LSc/r, NDB, MPO, AHN, VMH, IPN,
562 and CB.
563
564

Figure 6.

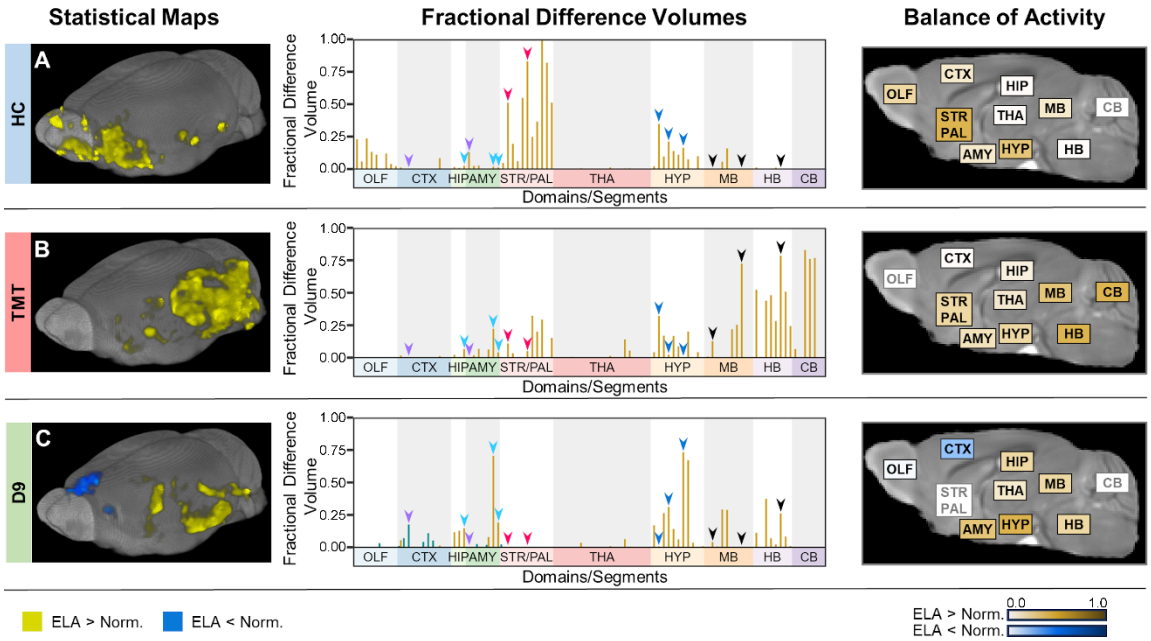

Fig. 6. Differences in brain state between ELA and Normal under three serial conditions. (***A-C***) From left to right: Left panels, statistical maps; Middle, corresponding column graphs; Right, diagrams of distributed pattern of brain-wide activity showing differences between groups at each condition. Color coding: ELA > Normal, yellow; Normal > ELA, blue. From top to bottom: (***A***) HC, (***B***) TMT, and (***C***) D9.

Left panels: 3D renderings of two-tailed unpaired t-tests of ELA vs Normal at each condition on anatomy of grayscale template ($T_{(22)}$ = 2.51 - 4.45, $p < 0.01 – 0.0001$, *cluster corr.*, n = 24).

Middle: Fractional difference volumes. Arrowheads indicate segments with interesting dynamics: ACB, LSr (pink), also measured by ROI in **Fig. 3**); MPO, AHN, VMH (dark blue); PA, COA, CA1-CA3 (turquoise); PL, AAA (purple); and VTA, CS, LC, monoaminergic nuclei (black). See ***SI Appendix*** **Table S5** for ordered list of segments and **Table S7** for fractional difference volume values.

Right: Diagrams of approximate anatomical location of domains with differing activity over the three conditions. Intensity of color fill proportional to the magnitude of fractional difference volumes (darkness/luminosity). See **Table 1** for individual segments with the greatest contributions.

585 **Table 1.** Segments with large contributions to differences in brain state between ELA and Normal.

Condition	Anatomical Domains	ELA > Normal (Segments)	ELA < Normal (Segments)
HC	STR/PAL	MS, LSr, NDB, LSc, ACB, BST, SI	-
	HYP	MPO	-
TMT	MB	CS	-
	HB	LC, P, MedOblog, PRN, PCG	-
	CB	PYR, UVU, NOD	-
D9	CTX	-	PL, MO
	AMY	*PA*	-
	HYP	*VMH, DMH, AHN, P/PeVH*	-
	MB	SNc, SNr	-
	HB	PCG, LC	-

586 Segments are ordered from left to right by magnitude of fractional difference volume, for each
587 domain, and separately for each direction of the t-test comparison.

588

589 **References**

590

591 1. Felitti VJ*, et al.* (1998) Relationship of Childhood Abuse and Household Dysfunction to
592 Many of the Leading Causes of Death in Adults. *American Journal of Preventive*
593 *Medicine* 14(4):245-258.
594 2. Merrick M*, et al.* (2019) Vital Signs: Estimated Proportion of Adult Health Problems
595 Attributable to Adverse Childhood Experiences and Implications for Prevention — 25
596 States, 2015–2017. *MMWR. Morbidity and Mortality Weekly Report* 68.
597 3. Zarse EM*, et al.* (2019) The adverse childhood experiences questionnaire: Two decades
598 of research on childhood trauma as a primary cause of adult mental illness, addiction,
599 and medical diseases. *Cogent Medicine* 6(1):1581447.
600 4. Spadoni AD*, et al.* (2022) Contribution of early-life unpredictability to neuropsychiatric
601 symptom patterns in adulthood. *Depression and Anxiety* 39(10-11):706-717.
602 5. Yehuda R*, et al.* (2010) Putative biological mechanisms for the association between early
603 life adversity and the subsequent development of PTSD. *Psychopharmacology*
604 212(3):405-417.
605 6. Birnie MT*, et al.* (2020) Plasticity of the Reward Circuitry After Early-Life Adversity:
606 Mechanisms and Significance. *Biological Psychiatry* 87(10):875-884.
607 7. Malave L, Van Dijk MT, & Anacker C (2022) Early life adversity shapes neural circuit
608 function during sensitive postnatal developmental periods. *Translational Psychiatry*
609 12(1):306.
610 8. Murthy S & Gould E (2020) How Early Life Adversity Influences Defensive Circuitry.
611 *Trends in Neurosciences* 43(4):200-212.
612 9. Smith KE & Pollak SD (2020) Early life stress and development: potential mechanisms
613 for adverse outcomes. *Journal of Neurodevelopmental Disorders* 12(1):34.
614 10. Duffy KA, McLaughlin KA, & Green PA (2018) Early life adversity and health-risk
615 behaviors: proposed psychological and neural mechanisms. 1428(1):151-169.
616 11. Silva BA, Gross CT, & Graff J (2016) The neural circuits of innate fear: detection,
617 integration, action, and memorization. *Learn Mem* 23(10):544-555.
618 12. Tovote P, Fadok JP, & Luthi A (2015) Neuronal circuits for fear and anxiety. *Nat Rev*
619 *Neurosci* 16(6):317-331.
620 13. Berridge Kent C & Kringelbach Morten L (2015) Pleasure Systems in the Brain. *Neuron*
621 86(3):646-664.
622 14. Russo SJ & Nestler EJ (2013) The brain reward circuitry in mood disorders. *Nature*
623 *Reviews Neuroscience* 14(9):609-625.

15. Molet J, Maras PM, Avishai-Eliner S, & Baram TZ (2014) Naturalistic rodent models of chronic early-life stress. *Developmental Psychobiology* 56(8):1675-1688.
16. Rice CJ, Sandman CA, Lenjavi MR, & Baram TZ (2008) A Novel Mouse Model for Acute and Long-Lasting Consequences of Early Life Stress. *Endocrinology* 149(10):4892-4900.
17. Bolton JL, Short AK, Simeone KA, Daglian J, & Baram TZ (2019) Programming of Stress-Sensitive Neurons and Circuits by Early-Life Experiences. 13.
18. Gunn BG*, et al.* (2013) Dysfunctional astrocytic and synaptic regulation of hypothalamic glutamatergic transmission in a mouse model of early-life adversity: relevance to neurosteroids and programming of the stress response. *The Journal of neuroscience : the official journal of the Society for Neuroscience* 33(50):19534-19554.
19. Evans GW*, et al.* (2016) Childhood Cumulative Risk Exposure and Adult Amygdala Volume and Function. *Journal of Neuroscience Research* 94(6):535-543.
20. Javanbakht A*, et al.* (2015) Childhood Poverty Predicts Adult Amygdala and Frontal Activity and Connectivity in Response to Emotional Faces. 9.
21. van Harmelen A-L*, et al.* (2014) Hypoactive medial prefrontal cortex functioning in adults reporting childhood emotional maltreatment. *Social Cognitive and Affective Neuroscience* 9(12):2026-2033.
22. Weissman DG*, et al.* (2020) Altered Neural Processing of Threat-Related Information in Children and Adolescents Exposed to Violence: A Transdiagnostic Mechanism Contributing to the Emergence of Psychopathology. *Journal of the American Academy of Child & Adolescent Psychiatry* 59(11):1274-1284.
23. Hanson JL, Williams AV, Bangasser DA, & Peña CJ (2021) Impact of Early Life Stress on Reward Circuit Function and Regulation. 12.
24. Aoki I, Wu YJ, Silva AC, Lynch RM, & Koretsky AP (2004) In vivo detection of neuroarchitecture in the rodent brain using manganese-enhanced MRI. *Neuroimage* 22(3):1046-1059.
25. Uselman TW, Medina CS, Gray HB, Jacobs RE, & Bearer EL (2022) Longitudinal manganese-enhanced magnetic resonance imaging of neural projections and activity.e4675.
26. Yu X, Sanes DH, Aristizabal O, Wadghiri YZ, & Turnbull DH (2007) Large-scale reorganization of the tonotopic map in mouse auditory midbrain revealed by MRI. *Proceedings of the National Academy of Sciences* 104(29):12193-12198.
27. Yu X, Wadghiri YZ, Sanes DH, & Turnbull DH (2005) In vivo auditory brain mapping in mice with Mn-enhanced MRI. *Nature Neuroscience* 8(7):961-968.

658 28. Malkova NV, Gallagher JJ, Yu CZ, Jacobs RE, & Patterson PH (2014) Manganese-
659 enhanced magnetic resonance imaging reveals increased DOI-induced brain activity in a
660 mouse model of schizophrenia. *Proc Natl Acad Sci U S A* 111(24):E2492-2500.
661 29. Uselman TW, Barto DR, Jacobs RE, & Bearer EL (2020) Evolution of brain-wide activity
662 in the awake behaving mouse after acute fear by longitudinal manganese-enhanced MRI.
663 *Neuroimage* 222:116975.
664 30. Bearer EL*, et al.* (2007) Role of neuronal activity and kinesin on tract tracing by
665 manganese-enhanced MRI (MEMRI). *Neuroimage* 37 Suppl 1:S37-46.
666 31. Bearer EL, Zhang X, & Jacobs RE (2007) Live imaging of neuronal connections by
667 magnetic resonance: Robust transport in the hippocampal–septal memory circuit in a
668 mouse model of Down syndrome. *NeuroImage* 37(1):230-242.
669 32. Medina CS*, et al.* (2019) Decoupling the Effects of the Amyloid Precursor Protein From
670 Amyloid-beta Plaques on Axonal Transport Dynamics in the Living Brain. *Front Cell*
671 *Neurosci* 13:501.
672 33. Pautler RG, Mongeau R, & Jacobs RE (2003) In vivo trans-synaptic tract tracing from the
673 murine striatum and amygdala utilizing manganese enhanced MRI (MEMRI). 50(1):33-
674 39.
675 34. Pautler RG, Silva AC, & Koretsky AP (1998) In vivo neuronal tract tracing using
676 manganese-enhanced magnetic resonance imaging. 40(5):740-748.
677 35. Tindemans I, Verhoye M, Balthazart J, & Van Der Linden A (2003) In vivo dynamic ME-
678 MRI reveals differential functional responses of RA- and area X-projecting neurons in the
679 HVC of canaries exposed to conspecific song. *The European journal of neuroscience*
680 18(12):3352-3360.
681 36. Van der Linden A, Van Meir V, Tindemans I, Verhoye M, & Balthazart J (2004)
682 Applications of manganese-enhanced magnetic resonance imaging (MEMRI) to image
683 brain plasticity in song birds. *NMR Biomed* 17(8):602-612.
684 37. Van der Linden A*, et al.* (2002) In vivo manganese-enhanced magnetic resonance
685 imaging reveals connections and functional properties of the songbird vocal control
686 system. *Neuroscience* 112(2):467-474.
687 38. Bedenk BT*, et al.* (2018) Mn(2+) dynamics in manganese-enhanced MRI (MEMRI):
688 Cav1.2 channel-mediated uptake and preferential accumulation in projection terminals.
689 *Neuroimage* 169:374-382.
690 39. Narita K, Kawasaki F, & Kita H (1990) Mn and Mg influxes through Ca channels of motor
691 nerve terminals are prevented by verapamil in frogs. *Brain research* 510(2):289-295.

692 40. Lin YJ & Koretsky AP (1997) Manganese ion enhances T1-weighted MRI during brain
693 activation: an approach to direct imaging of brain function. *Magnetic resonance in*
694 *medicine* 38(3):378-388.
695 41. Svehla P, Bedecarrats A, Jahn C, Nargeot R, & Ciobanu L (2018) Intracellular
696 manganese enhanced MRI signals reflect the frequency of action potentials in Aplysia
697 neurons. *J Neurosci Methods* 295:121-128.
698 42. Vousden DA*, et al.* (2018) Continuous manganese delivery via osmotic pumps for
699 manganese-enhanced mouse MRI does not impair spatial learning but leads to skin
700 ulceration. *NeuroImage* 173:411-420.
701 43. Fendt M, Endres T, Lowry CA, Apfelbach R, & McGregor IS (2005) TMT-induced
702 autonomic and behavioral changes and the neural basis of its processing. *Neuroscience*
703 *and biobehavioral reviews* 29(8):1145-1156.
704 44. Goswami S, Rodríguez-Sierra O, Cascardi M, & Pare D (2013) Animal models of post-
705 traumatic stress disorder: face validity. 7.
706 45. Rosen J, Asok A, & Chakraborty T (2015) The smell of fear: innate threat of 2,5-dihydro-
707 2,4,5-trimethylthiazoline, a single molecule component of a predator odor. 9.
708 46. Bhattacharyya PK, Phillips MD, Stone LA, & Lowe MJ (2017) Activation volume vs BOLD
709 signal change as measures of fMRI activation – Its impact on GABA – fMRI activation
710 correlation. *Magnetic Resonance Imaging* 42:123-129.
711 47. Kimbrough A*, et al.* (2020) Brain-wide functional architecture remodeling by alcohol
712 dependence and abstinence. 117(4):2149-2159.
713 48. Renier N*, et al.* (2016) Mapping of Brain Activity by Automated Volume Analysis of
714 Immediate Early Genes. *Cell* 165(7):1789-1802.
715 49. Greene AS, Horien C, Barson D, Scheinost D, & Constable RT (2023) Why is everyone
716 talking about brain state? *Trends Neurosci* 46(7):508-524.
717 50. Gallo M*, et al.* (2019) Limited Bedding and Nesting Induces Maternal Behavior
718 Resembling Both Hypervigilance and Abuse. 13.
719 51. Kundakovic M, Lim S, Gudsnuk K, & Champagne FA (2013) Sex-Specific and Strain-
720 Dependent Effects of Early Life Adversity on Behavioral and Epigenetic Outcomes.
721 *Frontiers in Psychiatry* 4.
722 52. Ashburner J*, et al.* (2012) SPM8 manual.
723 53. Ashburner J*, et al.* (2014) SPM12 manual. 2464(4).
724 54. Matsukawa M, Yoshikawa M, Katsuyama N, Aizawa S, & Sato T (2022) The Anterior
725 Piriform Cortex and Predator Odor Responses: Modulation by Inhibitory Circuits. *Front*
726 *Behav Neurosci* 16:896525.

727 55. Takahashi LK (2014) Olfactory systems and neural circuits that modulate predator odor
728 fear. *Front Behav Neurosci* 8:72.
729 56. Motta SC*, et al.* (2009) Dissecting the brain's fear system reveals the hypothalamus is
730 critical for responding in subordinate conspecific intruders. *Proceedings of the National*
731 *Academy of Sciences* 106(12):4870-4875.
732 57. Bath KG (2020) Synthesizing Views to Understand Sex Differences in Response to Early
733 Life Adversity. *Trends Neurosci* 43(5):300-310.
734 58. Ben-Shaul Y, Katz LC, Mooney R, & Dulac C (2010) In vivo vomeronasal stimulation
735 reveals sensory encoding of conspecific and allospecific cues by the mouse accessory
736 olfactory bulb. 107(11):5172-5177.
737 59. Canteras NS (2002) The medial hypothalamic defensive system: Hodological
738 organization and functional implications. *Pharmacology Biochemistry and Behavior*
739 71(3):481-491.
740 60. Canteras NS, Chiavegatto S, Ribeiro do Valle LE, & Swanson LW (1997) Severe
741 Reduction of Rat Defensive Behavior to a Predator by Discrete Hypothalamic Chemical
742 Lesions. *Brain Research Bulletin* 44(3):297-305.
743 61. Janitzky K, D′Hanis W, Kröber A, & Schwegler H (2015) TMT predator odor activated
744 neural circuit in C57BL/6J mice indicates TMT-stress as a suitable model for
745 uncontrollable intense stress. *Brain research* 1599:1-8.
746 62. Kunwar PS*, et al.* (2015) Ventromedial hypothalamic neurons control a defensive
747 emotion state. *eLife* 4:e06633.
748 63. Pérez-Gómez A*, et al.* (2015) Innate Predator Odor Aversion Driven by Parallel Olfactory
749 Subsystems that Converge in the Ventromedial Hypothalamus. *Current Biology*
750 25(10):1340-1346.
751 64. Koob GF & Volkow ND (2016) Neurobiology of addiction: a neurocircuitry analysis. *The*
752 *lancet. Psychiatry* 3(8):760-773.
753 65. Grandjean J*, et al.* (2020) Common functional networks in the mouse brain revealed by
754 multi-centre resting-state fMRI analysis. *Neuroimage* 205:116278.
755 66. Mandino F*, et al.* (2022) A triple-network organization for the mouse brain. *Molecular*
756 *Psychiatry* 27(2):865-872.
757 67. Alves PN, Forkel SJ, Corbetta M, & Thiebaut de Schotten M (2022) The subcortical and
758 neurochemical organization of the ventral and dorsal attention networks.
759 *Communications Biology* 5(1):1343.
760 68. Bell PT & Shine JM (2016) Subcortical contributions to large-scale network
761 communication. *Neuroscience & Biobehavioral Reviews* 71:313-322.

762 69. Durieux L*, et al.* (2022) Functional brain-wide network mapping during acute stress
763 exposure in rats: Interaction between the lateral habenula and cortical, amygdalar,
764 hypothalamic and monoaminergic regions. 56(8):5154-5176.
765 70. Salvan P*, et al.* (2023) Serotonin regulation of behavior via large-scale neuromodulation
766 of serotonin receptor networks. *Nature Neuroscience* 26(1):53-63.
767 71. Taylor NL*, et al.* (2022) Structural connections between the noradrenergic and cholinergic
768 system shape the dynamics of functional brain networks. *NeuroImage* 260:119455.
769 72. Tye KM (2018) Neural Circuit Motifs in Valence Processing. *Neuron* 100(2):436-452.
770 73. Vander Weele CM*, et al.* (2018) Dopamine enhances signal-to-noise ratio in cortical-
771 brainstem encoding of aversive stimuli. *Nature* 563(7731):397-401.
772 74. Zerbi V*, et al.* (2019) Rapid Reconfiguration of the Functional Connectome after
773 Chemogenetic Locus Coeruleus Activation. *Neuron* 103(4):702-718.e705.
774 75. Suri D, Teixeira CM, Cagliostro MKC, Mahadevia D, & Ansorge MS (2015) Monoamine-
775 Sensitive Developmental Periods Impacting Adult Emotional and Cognitive Behaviors.
776 *Neuropsychopharmacology* 40(1):88-112.
777 76. Wadghiri YZ*, et al.* (2004) Manganese-enhanced magnetic resonance imaging (MEMRI)
778 of mouse brain development. *NMR in Biomedicine* 17(8):613-619.
779 77. Coletta L*, et al.* (2020) Network structure of the mouse brain connectome with voxel
780 resolution. 6(51):eabb7187.
781 78. Hillhouse TM & Porter JH (2015) A brief history of the development of antidepressant
782 drugs: From monoamines to glutamate. *Experimental and Clinical Psychopharmacology*
783 23(1):1-21.
784 79. O'Donnell JM, Bies RR, & Shelton RC (2017) Drug Therapy of Depression and Anxiety
785 Disorders. *Goodman & Gilman's: The Pharmacological Basis of Therapeutics, 13e*,
786 eds Brunton LL, Hilal-Dandan R, & Knollmann BC (McGraw-Hill Education, New York,
787 NY).
788 80. Pereira VS & Hiroaki-Sato VA (2018) A brief history of antidepressant drug development:
789 from tricyclics to beyond ketamine. *Acta Neuropsychiatrica* 30(6):307-322.
790 81. Hakamata Y, Suzuki Y, Kobashikawa H, & Hori H (2022) Neurobiology of early life
791 adversity: A systematic review of meta-analyses towards an integrative account of its
792 neurobiological trajectories to mental disorders. *Frontiers in Neuroendocrinology*
793 65:100994.
794 82. Karcher NR & Barch DM (2021) The ABCD study: understanding the development of risk
795 for mental and physical health outcomes. *Neuropsychopharmacology* 46(1):131-142.

83. Price JC, Lee JJ, Saraiya N, Lei S, & Mintz CD (2023) An Update on NIH Programs Relevant to Child Brain Health Research: ECHO, ABCD, HBCD, and MIRA. 35(1):119-123.
84. Barron HC, Mars RB, Dupret D, Lerch JP, & Sampaio-Baptista C (2021) Cross-species neuroscience: closing the explanatory gap. 376(1815):20190633.
85. Lehallier B*, et al.* (2012) Brain Processing of Biologically Relevant Odors in the Awake Rat, as Revealed by Manganese-Enhanced MRI. *PLoS ONE* 7(10):e48491.
86. Petrus E, Saar G, Daoust A, Dodd S, & Koretsky AP (2021) A hierarchy of manganese competition and entry in organotypic hippocampal slice cultures. *NMR in Biomedicine* 34(4).
87. Manzano Nieves G, Bravo M, & Bath KG (2023) Early life adversity ablates sex differences in active versus passive threat responding in mice. *Stress*:1-32.
88. Spring S, Lerch JP, & Henkelman RM (2007) Sexual dimorphism revealed in the structure of the mouse brain using three-dimensional magnetic resonance imaging. *NeuroImage* 35(4):1424-1433.
89. Bruce MR*, et al.* (2021) Sexually dimorphic neuroanatomical differences relate to ASD-relevant behavioral outcomes in a maternal autoantibody mouse model. *Molecular Psychiatry* 26(12):7530-7537.
90. Holz NE*, et al.* (2023) A stable and replicable neural signature of lifespan adversity in the adult brain. *Nature Neuroscience*.
91. Lerch JP*, et al.* (2011) Maze training in mice induces MRI-detectable brain shape changes specific to the type of learning. *NeuroImage* 54(3):2086-2095.
92. Murthy S & Gould E (2018) Early Life Stress in Rodents: Animal Models of Illness or Resilience? 12.
93. Peña CJ, Nestler EJ, & Bagot RC (2019) Environmental Programming of Susceptibility and Resilience to Stress in Adulthood in Male Mice. 13.
94. Shemesh Y & Chen A (2023) A paradigm shift in translational psychiatry through rodent neuroethology. *Molecular Psychiatry* 28(3):993-1003.
95. Verbitsky A, Dopfel D, & Zhang N (2020) Rodent models of post-traumatic stress disorder: behavioral assessment. *Translational Psychiatry* 10(1).
96. McLaughlin KA, Sheridan MA, Humphreys KL, Belsky J, & Ellis BJ (2021) The Value of Dimensional Models of Early Experience: Thinking Clearly About Concepts and Categories. *Perspect Psychol Sci* 16(6):1463-1472.
97. Packard K & Opendak M (2022) Rodent models of early adversity: Impacts on developing social behavior circuitry and clinical implications. 16.

98. Brigman JL, Mathur P, Lu L, Williams RW, & Holmes A (2009) Genetic relationship between anxiety-related and fear-related behaviors in BXD recombinant inbred mice. 20(2):204-209.
99. Noldus LPJJ, Spink AJ, & Tegelenbosch RAJ (2001) EthoVision: A versatile video tracking system for automation of behavioral experiments. *Behavior Research Methods, Instruments, & Computers* 33(3):398-414.
100. Fox J & Weisberg S (2019) An R Companion to Applied Regression.
101. Lenth RV (2022) emmeans: Estimated Marginal Means, aka Least-Squares Means.
102. Pinheiro J, Bates D, & Team RC (2022) nlme: Linear and Nonlinear Mixed Effects Models.
103. Pinheiro JC & Bates DM (2000) Mixed-Effects Models in S and S-PLUS.
104. Posit t (2022) RStudio: Integrated Development Environment for R.
105. Team RC (2022) R: A Language and Environment for Statistical Computing.
106. Wickham H (2016) ggplot2: Elegant Graphics for Data Analysis.
107. Gallagher JJ*, et al.* (2013) Altered reward circuitry in the norepinephrine transporter knockout mouse. *PLoS One* 8(3):e57597.
108. Zhang X*, et al.* (2010) Altered neurocircuitry in the dopamine transporter knockout mouse brain. *PLoS One* 5(7):e11506.
109. Frahm J, Haase A, & Matthaei D (1986) Rapid NMR imaging of dynamic processes using the FLASII technique. 3(2):321-327.
110. Haase A, Frahm J, Matthaei D, Hanicke W, & Merboldt KD (1986) FLASH imaging. Rapid NMR imaging using low flip-angle pulses. *Journal of Magnetic Resonance (1969)* 67(2):258-266.
111. Medina CS, Manifold-Wheeler B, Gonzales A, & Bearer EL (2017) Automated Computational Processing of 3-D MR Images of Mouse Brain for Phenotyping of Living Animals. *Curr Protoc Mol Biol* 119:29A 25 21-29A 25 38.
112. Delora A*, et al.* (2016) A simple rapid process for semi-automated brain extraction from magnetic resonance images of the whole mouse head. *J Neurosci Methods* 257:185-193.
113. Sled JG, Zijdenbos AP, & Evans AC (1998) A nonparametric method for automatic correction of intensity nonuniformity in MRI data. *IEEE Trans Med Imaging* 17(1):87-97.
114. Jenkinson M, Beckmann CF, Behrens TE, Woolrich MW, & Smith SMJN (2012) Fsl. 62(2):782-790.
115. Jenkinson M, Bannister P, Brady M, & Smith S (2002) Improved optimization for the robust and accurate linear registration and motion correction of brain images. *Neuroimage* 17(2):825-841.

866 116. Jenkinson M & Smith S (2001) A global optimisation method for robust affine registration
867 of brain images. *Medical image analysis* 5(2):143-156.
868 117. Wickham H*, et al.* (2019) Welcome to the Tidyverse. 4(43):1686.
869 118. Tyszka JM, Readhead C, Bearer EL, Pautler RG, & Jacobs RE (2006) Statistical diffusion
870 tensor histology reveals regional dysmyelination effects in the shiverer mouse mutant.
871 *NeuroImage* 29(4):1058-1065.

872